

Analysis of work hardening mechanisms in Quenching and Partitioning steels combining experiments with a 3D micro-mechanical model

Celada-Casero, Carola; Vercruyssen, Florian; Linke, Bernd; Smith, Ali; Kok, Piet; Sietsma, Jilt; Santofimia, Maria Jesus

DOI

[10.1016/j.msea.2022.143301](https://doi.org/10.1016/j.msea.2022.143301)

Publication date

2022

Document Version

Final published version

Published in

Materials Science and Engineering A

Citation (APA)

Celada-Casero, C., Vercruyssen, F., Linke, B., Smith, A., Kok, P., Sietsma, J., & Santofimia, M. J. (2022). Analysis of work hardening mechanisms in Quenching and Partitioning steels combining experiments with a 3D micro-mechanical model. *Materials Science and Engineering A*, 846, Article 143301. <https://doi.org/10.1016/j.msea.2022.143301>

Important note

To cite this publication, please use the final published version (if applicable). Please check the document version above.

Copyright

Other than for strictly personal use, it is not permitted to download, forward or distribute the text or part of it, without the consent of the author(s) and/or copyright holder(s), unless the work is under an open content license such as Creative Commons.

Takedown policy

Please contact us and provide details if you believe this document breaches copyrights. We will remove access to the work immediately and investigate your claim.



Analysis of work hardening mechanisms in Quenching and Partitioning steels combining experiments with a 3D micro-mechanical model

Carola Celada-Casero^{a,b,*}, Florian Verccruysse^c, Bernd Linke^d, Ali Smith^e, Piet Kok^{c,f}, Jilt Sietsma^a, Maria Jesus Santofimia^a

^a Department of Materials Science and Engineering, Delft University of Technology, Mekelweg 2, 2628 CD, Delft, the Netherlands

^b Department of Physical Metallurgy, Spanish National Center for Metallurgical Research (CENIM-CSIC), Avda. Gregorio del Amo 8, E-28040, Madrid, Spain

^c Department of Electromechanical, Systems & Metal Engineering, Research Group Materials Science and Technology, Ghent University, Tech Lane Science Park Campus A, 9052, Zwijnaarde, Belgium

^d ThyssenKrupp Steel Europe AG, Kaiser-Wilhelm-Strasse 100, Duisburg, DE-47166, Germany

^e Rina Consulting, Centro Sviluppo Materiali SpA, Via di Castel Romano 100, Rome, 00128, Italy

^f Tata Steel, P.O. Box 10000, 1970, CA, IJmuiden, the Netherlands

ARTICLE INFO

Keywords:

3D micromechanical modeling
Crystal plasticity
RVE
Work hardening
Martensite
Austenite
TRIP effect
Q&P microstructures

ABSTRACT

Quenching & Partitioning (Q&P) steels owe their good strength-ductility combinations to the martensite/austenite (α'/γ) mechanical interactions and to the formation of mechanically-induced martensite (α'_{mech}) through the transformation-induced plasticity (TRIP) effect. An essential role is played by carbon, whose distribution among the phases can be modified through the Q&P route. This study presents a methodology to systematically and quantitatively examine the influence of the α'/γ mechanical interactions on the overall work hardening of the steel with respect to the role of carbon in the martensite. The methodology rests on the generation of a 3D micro-mechanical model that allows to derive, by crystal plasticity simulations, the overall response of a mechanically-stable α'/γ virtual microstructure. In combination with theoretical knowledge on hardening, the comparison between the experimental and simulated mechanical responses enables the quantification of the influence of the martensite carbon content and distribution on the overall TRIP strengthening contribution of the steel. The approach is applied to two low carbon Q&P-processed α'/γ microstructures of similar initial volume fractions of austenite and α'_{mech} formation kinetics with strain, but one containing a Nb-microaddition and displaying improved strength-ductility values. It is shown that the martensite strength and work hardening ability might additionally enhance or partially counteract the strengthening contribution from the austenite-to- α'_{mech} transformation during uniaxial loading. The results of this study highlight that the processing-dependent properties of the carbon-depleted martensite should be considered in the optimization of Q&P processed steels.

1. Introduction

The need for steel designs with increasing levels of high strength, ductility and formability at room temperature is in the spotlight to favor automotive light weighting, energy saving during manufacturing and environmental sustainability [1]. In this regard, Quenching & Partitioning (Q&P) steels [2,3] have demonstrated to provide strength, toughness and improved work hardening and ductility with respect to dual-phase (DP) steels. The mechanical response of Q&P

microstructures relies on the physical interactions between the constituent phases during loading, i.e. carbon-depleted martensite and finely dispersed metastable retained austenite (RA). Phase interactions are caused by the stress and strain partitioning and depend on the composition and the microstructure topology, i.e. grain size, morphology and phase spatial distribution [4–6].

In the trend to optimize the mechanical properties and performance of Q&P steels, major attention has been paid to attain the maximum volume fraction of austenite to exploit the transformation-induced plasticity (TRIP) effect, i.e. necking delay due to the progressive

* Corresponding author. Delft University of Technology, Mekelweg 2, 2628 CD, Delft, the Netherlands.

E-mail addresses: C.CeladaCasero@tudelft.nl, c.celada@cenim.csic.es (C. Celada-Casero), Florian.Verccruysse@UGent.be (F. Verccruysse), Bernd.Linke@thyssenkrupp.com (B. Linke), Ali.Smith@rina.org (A. Smith), Piet.Kok@UGent.be (P. Kok), J.Sietsma@tudelft.nl (J. Sietsma), M.J.SantofimiaNavarro@tudelft.nl (M.J. Santofimia).

<https://doi.org/10.1016/j.msea.2022.143301>

Received 24 November 2021; Received in revised form 6 April 2022; Accepted 11 May 2022

Available online 14 May 2022

0921-5093/© 2022 The Authors. Published by Elsevier B.V. This is an open access article under the CC BY license (<http://creativecommons.org/licenses/by/4.0/>).

Nomenclature			
α	Fitting parameter of the forest dislocation strengthening contribution	$\Delta\sigma^T$	(Exp-Sim) Experimental-numerical TRIP strengthening deviation
α'	Martensite	$\Delta\sigma^T(\epsilon)$	Theoretical TRIP strengthening increment due to the formation of mechanically-induced martensite with strain
α'_{mech}	Mechanically-induced martensite	$\Delta\theta_{M1}$	TRIP strengthening increment due to the mechanical contribution from primary martensite
γ	Austenite	a	Crystal plasticity hardening numerical value
$\dot{\gamma}_0$	Initial shear rate	a_γ	Austenite lattice parameter
ϵ_e	Engineering strain	b	Burgers vector
ϵ_t	Total elongation	C_{kl}	Elastic stiffness constants
ϵ_T	True strain	d_i	Grain size of phase i
ϵ_{un}	Uniform elongation	f_i	Volume fraction of phase i
θ	Work hardening rate	f_{RA}^F	Volume fraction of RA near necked region
ρ	Dislocation density	G	Shear modulus
σ_0	Lattice friction stress for pure Fe	h_0	Initial hardening parameter
σ_C	Overall carbon strengthening contribution	k_{HP}	Hall-Petch coefficient
$\sigma_{C\ ss}$	Solid solution strengthening of carbon	M	Misorientation factor
σ_{st}	Solid solution strengthening contribution of substitutional alloying elements	n	Strain rate sensitivity parameter
σ_e	Engineering stress	T_Q	Quenching temperature
σ_{GB}	Grain boundary strengthening contribution	CP	Crystal Plasticity
σ_ρ	Forest dislocation strengthening contribution	DAMASK	Düsseldorf Advanced Material Simulation Kit
$\sigma_{ppt-\epsilon}$	Precipitation strengthening from ϵ -carbides	EBSD	Electron backscatter diffraction
$\sigma_{ppt-NbC}$	Precipitation strengthening from NbC carbides	EDS	Energy-dispersive X-ray spectroscopy
σ_T	True stress	FFT	Fast Fourier transform
σ_{ys}^i	Yield strength of phase i	IPF	Inverse Pole Figure
$\sigma_{ys}^{Q\&P}$	Yield strength of the Q&P steels	ODF	Orientation Distribution Function
τ	Critical resolved shear stress of a single crystal	M1	Primary martensite
$\tau_{c,0}$	Initial critical slip resistance	PAGS	Prior austenite grain size
τ_{sat}	Saturation slip resistance	Q&P	Quenching and Partitioning
φ	Grain size ratio	RVE	Representative volume element
x_c^i	Carbon content of phase i (in wt. %)	RA	Retained austenite
x_j	Content of alloying element j (in wt. %)	SEM	Scanning electron microscopy
$x_{C\ ppt-NbC}$	Carbon content in NbC precipitates	TRIP	Transformation-induced plasticity
$x_{C\ ppt-\epsilon}$	Carbon content in ϵ -carbides	TEM	Transmission Electron Microscopy
$x_{C\ ss}$	Carbon content in solid solution	UTS	Ultimate tensile strength
X_C^{Steel}	Nominal carbon content of the steel	XRD	X-ray diffraction
		YS _{0.2}	Yield strength (0.2% offset)

formation of mechanically-induced martensite (α'_{mech}) during straining [7–9]. Besides composition, morphology and grain size [10], the resistance of austenite to transform into α'_{mech} at room temperature is substantially influenced by the hydrostatic pressure exerted by the surrounding martensite [6,11,12]. Particularly, the presence of hard fresh martensite adjacent to austenite influences negatively the strain distribution, acting as a stress concentrator and leading to void nucleation [13,14]; while the presence of primary martensite with the appropriate strength might improve the accommodation of plastic deformation and the work hardening rate [15,16]. By means of *in-situ* high-energy synchrotron X-ray diffraction (HE-XRD) during monotonic tensile tests, Hidalgo et al. [16] showed that the formation kinetics of α'_{mech} in austenite/martensite structures is modified by changing the strength of the martensite relative to the austenite through tempering. It was concluded that the phase strength ratio significantly affects the stress/strain partitioning during loading, the work hardening of the individual phases and, thereby, the overall mechanical response of the microstructure. This implies that the strength of the carbon-depleted martensite is a key processing-dependent parameter for the design of Q&P steels with improved strength-ductility combinations. However, the microstructural features controlling the phase strength ratio in Q&P-processed microstructures are difficult to optimize given the complexity of physical processes involved in the thermal cycle [17–22]. Besides, the experimental study of Q&P microstructures optimization for

work hardening improvement turns out to be tedious by advanced characterization techniques like HE-XRD, and appears to be additionally hampered due to the small size of the retained austenite.

Alternatively to experiments, three-dimensional (3D) micro-mechanical models have been proven versatile to investigate the effect of controlled microstructure modifications on the stress/strain partitioning at the micro-scale and on the mechanical response of TRIP [23, 24] and DP steel grades [25,26]. The accuracy of 3D micromechanical models strongly relies on the realism of the 3D microstructure model, or representative volume element (RVE) [27–29], and on the description of the constitutive behavior of the individual phases and their interactions according to a certain crystal plasticity (CP) formulation. Through the 3D RVE, 3D micromechanical models capture the crystallographic orientations and microstructure topology parameters like phase fractions, grain size, spatial distribution and grain boundary morphology. There is sufficient experimental evidence of the significant influence of microstructure topological characteristics on the distribution of the stress and the strain and, thereby, on the overall work hardening of complex microstructures [4,6,28–30]. In this sense, 3D micromechanical models offer a tremendous advantage for the investigation of microstructure-properties relations in advanced high-strength steels (AHSS) with respect to classical continuum mechanical models.

Nevertheless, despite their potential, the application of 3D micro-mechanical models to Q&P and other AHSS is yet very scarce due to the

following main reasons [31]. First, the geometrical description at the grain level, and in three dimensions, of hierarchical structures like martensite poses a challenge for the creation of statistical RVEs. The compositional and grain size effects on the martensite morphology and crystallographic variant selection makes the development of suitable geometrical descriptors even more daunting. In addition, even if the 3D microstructure geometry modeling of complete hierarchical structures were possible, the calculation speed of currently-used methods would not enable the numerical computation of the high resolution RVE required to resolve the nanometer martensite laths or nanometer grains in a realistic time. Second, there is a lack of fundamental understanding of the constitutive behavior of the individual phases and the martensite/austenite mechanical interactions with respect to the processing thermal cycle. The description of these constitutive behaviors often requires a large number of fitting parameters accounting for the multiple active plastic deformation and strengthening mechanisms, i.e. dislocation glide, precipitation hardening, mechanical twinning (TWIP) or TRIP. This is particularly challenging for Q&P-processed microstructures.

This study presents a methodology to gain a deeper insight into the role of processing-dependent microstructural modifications in the intrinsic strength and work hardening ability of the individual martensite and austenite phases and their mechanical interactions. The emphasis is placed on the influence of the martensite carbon content and distribution, on the overall strengthening resulting from: 1) the austenite being replaced by the mechanically-induced martensite during uniaxial loading, and 2) the thus-induced work hardening in the surrounding martensite to accommodate the plastic deformation due to the lattice volume expansion associated to the martensitic transformation. The method is demonstrated for two low-carbon Q&P-processed α'/γ microstructures, one containing 0.025% Nb and displaying improved strength-ductility values. The two α'/γ microstructures contain similar initial volume fractions of austenite and have similar kinetics for mechanically-induced formation of martensite. This makes it an interesting study case to investigate, through the application of the presented methodology, the influence of the mechanical behavior of martensite on the overall work hardening of the steels. This knowledge will enable the optimization of Q&P-processed martensite/austenite microstructures.

2. Experimental-numerical methodology

Besides the initial volume fraction of austenite and its mechanically-induced decomposition kinetics, additional microstructure features influence the overall TRIP strengthening contribution in Q&P steels. Among these microstructure features, an essential role is played by the strength and work hardening ability of the primary martensite through the carbon content and distribution. A means to systematically and quantitatively examine the influence of the martensite strength on the work hardening resulting from the TRIP effect in α'/γ microstructures is to compare its overall mechanical response to that of a mechanically stable microstructure counterpart. However, the creation of such mechanically stable α'/γ microstructure containing austenite volume fractions representative of Q&P steels (0.10–0.25), is not feasible experimentally in the case of conventional low-carbon steels. Alternatively to experiments, we present a microstructure-based experimental-numerical method (Fig. 1) that allows to derive the mechanical response of a virtual mechanically stable α'/γ microstructure from microstructure-based crystal plasticity simulations. First, a three-dimensional statistically representative microstructure model, or 3D RVE, is created based on the microstructure topology and characterization data (Sections 2.1 and 2.2). Then, the RVE is subjected to a virtual mechanical test by crystal plasticity simulations, in which the austenite mechanical behavior is chosen to be that of a mechanically stable phase. Once the microstructure-based crystal plasticity simulations are completed, the integration of the computed internal variables provides the stress-strain response of the mechanically stable RVE (Section 2.3).

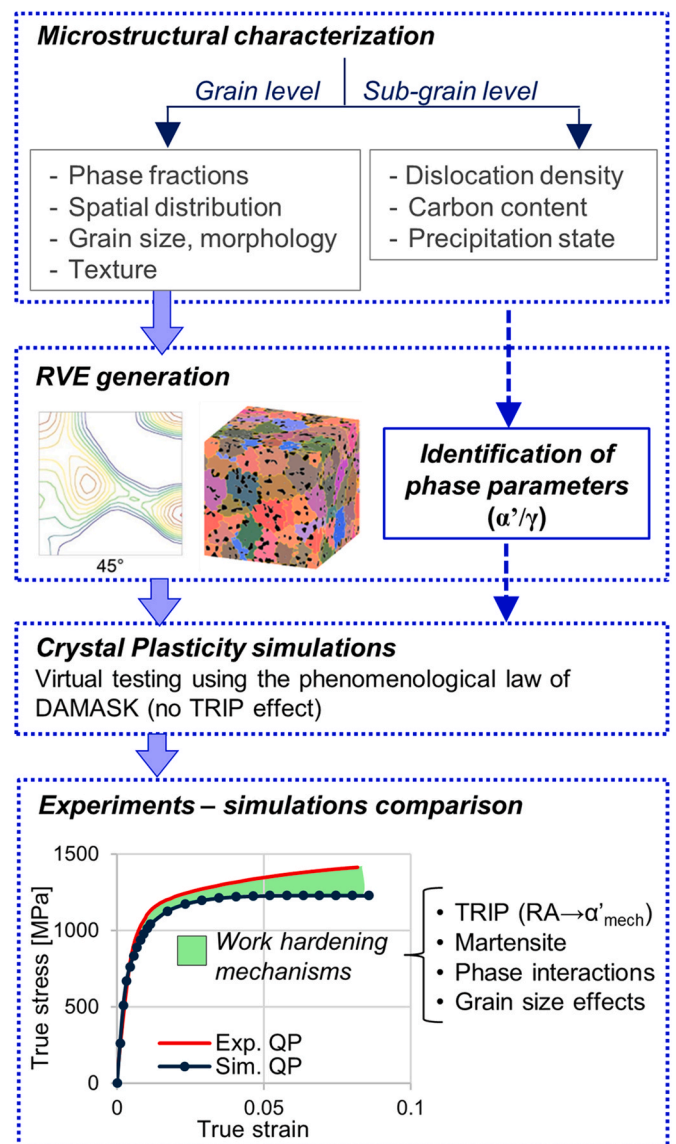


Fig. 1. Workflow of the proposed multi-scale experimental-numerical approach to investigate the strengthening contribution due to the formation of mechanically-induced martensite.

Finally, the simulated response is quantitatively compared to the experimental one (Section 2.4). Such comparison, in combination with theoretical knowledge on hardening, provides insight into the overall strengthening contribution resulting from α'/γ interactions in the steel, in relation with the primary martensite strength and work hardening ability.

2.1. Required microstructural characterization for the methodology

The development of 3D micromechanical models relies on an accurate characterization of the microstructure at the grain level (or micro-scale) and sub-grain level (or sub-micro-scale). The characterization data at the grain-level, like the crystallographic orientations and the microstructure topological data, such as phase fractions, spatial distribution and grain size, are used for the creation of statistically representative microstructure models. The characterization data at the sub-grain level, like the phase carbon content, dislocation density and precipitation state (in this study Nb-microalloyed Q&P steel is investigated) is essential to identify the material parameters that describe the mechanical properties and flow behavior of the individual phases. This sub-

grain microstructural information is incorporated in the micro-mechanical model through theoretical knowledge on hardening mechanisms (presented in Section 5.2.1 for the studied microstructures).

2.2. Generation of a microstructure model or RVE

The experimentally characterized crystallographic orientations, volume fractions, spatial distribution and averaged grain size values, by electron backscatter diffraction (EBSD), are used to create a periodic 3D RVE, i.e. a virtual model of the real microstructure. In this study, the multilevel Voronoi algorithm developed by Tata Steel is used for RVE generation [23,24,27]. Martensite/austenite microstructures are modelled under the following considerations: 1) the martensite block is considered as the effective strengthening unit and, thus, it is used to represent martensite grains in the RVE; 2) in the EBSD analysis, the martensite block boundaries are defined as those with a misorientation angle of 10° or higher [32]; 3) the martensite block and austenite grain sizes are defined as the average equivalent diameter of a circle with an equal grain area as measured with EBSD; 4) phase grains in the RVEs are spheres with an equal Voronoi cell volume and are characterized by a diameter equal to the experimental equivalent diameter.

Fig. 2 exemplifies the modeling process for the case of a martensite/austenite microstructure. Firstly, a periodic standard Voronoi diagram is created according to a randomly-generated point field (green tessellation in Fig. 2a). This constitutes a first-level tessellation. First-level Voronoi cells can be grouped according to a second spatial randomly-generated point field of lower density. All first-level cells whose seeds are located within a certain second-level cell are merged to form a single grain. This results in larger grains with complex-shaped grain boundaries (outlined in black in Fig. 2a and b), which will represent the martensite blocks, whereas the smaller, first-level cells, will represent the retained austenite grains. The ratio between the martensite block size (d_α) and the retained austenite grain size (d_γ), $\varphi = d_\alpha / d_\gamma$, can be thus modified by adjusting the first-to second-level point field densities. In this example, $\varphi = 5$. As representative of randomly generated standard Voronoi diagrams, all cells have an equiaxed morphology and a size within a Gaussian grain size distribution of the selected average grain size value (in this study, the experimental average grain sizes are used). Then, first-level cells are used to introduce a specific volume fraction of retained austenite grains with a certain spatial distribution. Fig. 2b displays in black a 0.14 vol fraction of randomly distributed retained austenite grains.

Finally, the multilevel Voronoi algorithm allows to assign realistic crystallographic orientations to the RVE phases following these steps: 1) the crystallographic orientations of the phases are characterized by EBSD, using the EBSD “average orientation” cleaning procedure. This provides a homogeneous, averaged, grain orientation value per

martensite block unit and austenite grain, i.e. a unique set of Euler angles in association with a grain area; 2) the set of grain orientation values for each phase are assigned to the corresponding phase in the RVE based on area-fraction weights through a Monte Carlo based optimization procedure to ensure a realistic texture representation. Fig. 2c shows the complete microstructure model, where the martensite and austenite crystallographic orientations are represented by RGB and greyscale colors, respectively. Once completed, the RVE is discretized into a regular grid of material points. For exemplification, Fig. 2d shows an RVE cross-section after discretization in 64^3 voxels. Each material point contains the information in accordance with the phase spatial distribution in the RVE.

A compromise between RVE size and RVE resolution should be established to optimize the computational effort. On the one hand, the RVE should be sufficiently large to guarantee that the collective response of the grains converges to the macroscopic bulk response of the material. On the other hand, the RVE resolution should be sufficiently high to ensure that the phase volume fractions and other characteristics remain unchanged after discretization. In α'/γ microstructures representative of Q&P-processed steels, the RVE resolution is given by the retained austenite grain size (the smallest phase).

2.3. Crystal plasticity simulations

The discretized RVE is interfaced to the open-source fast Fourier transform (FFT) spectral solver, coupled to the Düsseldorf Advanced Material Simulation Kit (DAMASK) [33] for crystal plasticity simulations. The phenomenological hardening law of DAMASK is used. It provides a constitutive description of defects evolution and the associated interaction laws describing strain hardening in individual deformation systems (see formulation in Ref. [34]). The FFT-based solver of DAMASK performs numerical simulations under periodic boundary conditions with a high convergence rate, satisfying strain compatibility within a reasonable time [35]. The computation of the internal variables is performed incrementally in time in each material point, for which the state of stress and strain is obtained. The integration of these stress and strain values results in the macroscopic stress-strain response of the RVE.

In this study, uniaxial virtual tensile tests were performed parallel to the RVE x-(rolling-) direction at a strain rate matching the experimental one ($8 \cdot 10^{-4} \text{ s}^{-1}$) and to a final strain level equal to the experimental uniform elongation of 0.08.

2.4. Experiment-simulation comparison

The tensile test simulation of a mechanically stable α'/γ microstructure model allows to observe the influence of the crystallographic orientations and microstructure features on the overall work hardening,

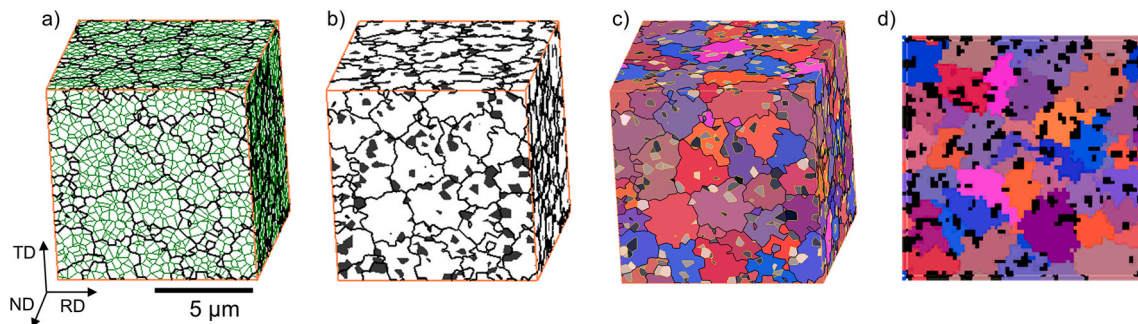


Fig. 2. 3D RVE generation of a Q&P microstructure using multilevel Voronoi tessellations. (a) First-level Voronoi cells (outlined in green) are grouped in grains (outlined in black) according to a coarser tessellation; (b) a 0.14 vol fraction of retained austenite particles is introduced in a random dispersion (black cells); (c) characteristic crystallographic orientations are assigned to martensite grains (in RGB colors) and to retained austenite particles (in greyscale); and (d) RVE cross section using a regular grid of 64^3 voxels, with the retained austenite particles colored in black. (For interpretation of the references to color in this figure legend, the reader is referred to the Web version of this article.)

without the influence exerted by the formation of mechanically-induced martensite. It is not possible to obtain such information by means of experiments in low-carbon α'/γ structures due to the relatively low metastability of the austenite phase. Combined with theoretical knowledge on hardening mechanisms, the comparison of the simulated and experimental mechanical responses provides quantitative information of the overall strengthening contribution derived from α'/γ interactions, in relation with the martensite strength and work hardening ability. This includes the role of the austenite being replaced by the mechanically-induced martensite and the thus-induced work hardening in the martensite to accommodate the plastic deformation resulting from the volume expansion associated to the martensitic transformation.

The presented experimental-numerical method offers a novel and unique opportunity to examine the role of microstructural modifications in the intrinsic strength of phases and their mechanical interactions. The method will aid the microstructural design optimization in Q&P steels and other advanced high-strength steels.

3. Materials and experimental procedure

The approach presented in Fig. 1 is applied to two Q&P-processed steels of composition 0.2C-1.25Si-2.4Mn-0.3Cr-0.02Al (in wt. %), one of them containing a micro-addition of 0.025 wt% Nb. The steels will be referred to as “Q&P” and “Nb-Q&P” throughout this study. The composition selection and manufacturing of the steel samples is detailed in a previous work of the authors [36]. The cold-rolled sheets were subjected to Q&P thermal cycles using a VATRON-4 thermal simulator (Fig. 3a). Characterization results in Ref. [36] revealed that volume fraction of fresh martensite in the final Q&P microstructures is lower than 0.02 ± 0.01 for both investigated Q&P steels. Thus, and for

microstructure modeling purposes, the studied microstructures are assumed to consist of carbon-depleted martensite (M1), formed during the first quench to the quenching temperature (T_Q), and retained austenite (RA).

Scanning electron microscopy (SEM) was used for the observation of the Q&P microstructures. SEM images were obtained using a JEOL JSM-6500F SEM operating at 14 kV. Sample surface preparation was done by grinding, polishing down to 1 μm and etching with a 2% Nital solution for 5 s. Electron backscatter diffraction (EBSD) and Transmission Electron Microscopy (TEM) were carried out at the facilities of the Department of Electromechanical, Systems & Metal Engineering of Ghent University, in Belgium. For microstructure quantification, an AMETEK EDAX-TSL EBSD system coupled to a Quanta 450 FEG-SEM was used, operating at 20 kV, 16 mm of working distance and a step size of 50 nm. Specimen surface preparation included an additional colloidal silica (OPS) polishing step after standard grinding and polishing. Data post-processing was carried out with the TSL-OIM Data analysis software v7.3. Grains were defined considering a minimum of 5 neighboring points and a grain tolerance angle of 5° . Additionally, clean-up procedures were applied in all cases: grain dilatation, grain confidence index standardization and single average orientation per grain. The characterization of the average grain sizes of martensite (d_{M1}) and retained austenite (d_{RA}), as well as the prior austenite grain size (PAGS) is detailed in a previous study [36]. The grain size was defined as the equivalent diameter of a circle with an equal grain area. Grain sizes are expressed as the average value, with the reported standard deviation being the uncertainty. The block martensite grain boundaries, with misorientation angles of 10° or higher, were used to define the martensite effective grain size [32]. TEM was used to determine the size of the nano-precipitates present in the Nb-containing steel. Discs of 3 mm in diameter were punched from the sheet previously thinned to 80–100 μm by mechanical grinding and polishing. The discs were electropolished using a twin-jet Struers Tenupol-5 and an electrolyte composed of 4% vol. HClO_4 in a 63% vol. acetic acid solution diluted in water.

X-ray diffraction (XRD) scans in the 2θ range 40° – 130° using a step size of 0.033° (2θ) and a counting time per step of 2 s were performed using $\text{Co K}\alpha$ radiation in a Bruker type d8-Advance diffractometer equipped with graphite monochromator and Vantec position sensitive detector. Rietveld refinement of diffractograms and data evaluation was done using the Bruker software DIFFRAC.EVA 4.2.2. To determine the volume fraction of retained austenite and its lattice parameter the procedure explained in Ref. [37] and the Nelson-Riley method [38] were applied. The uncertainties of the volume fractions are given by the average value of the ratio between the expected and the measured intensity of each particular austenite X-ray peak. The diffraction peaks from the tempered martensite of the samples are amenable to profile fitting with standard shape functions, yielding reliable integrated intensities [39]. The carbon content in the retained austenite (x_c^{RA}) was determined from Ref. [40]:

$$a_\gamma = 3.556 + 0.0453x_c^{RA} + 0.00095x_{Mn} + 0.0056x_{Al} \quad (1)$$

where x_i indicates content of alloying element i in phase austenite in wt. % and the lattice parameter a_γ is in Ångström. The uncertainties of x_c^{RA} were calculated from the standard error of the lattice parameter, calculated using the LINEST function of MS-Excel for the Nelson-Riley data.

Small tensile specimens, of the geometry shown in Fig. 3b, were machined by electrical discharge machining with the axial length parallel to the sheet rolling direction. Two specimens of each Q&P steel were tested to fracture at a strain rate of $8 \times 10^{-4} \text{ s}^{-1}$ using a Zwick Z100 testing frame, a 100 kN cell and an extensometer of 20 mm in gauge length. Additionally, one specimen of each Q&P steel was subjected to subsequent load-unload cycles in small strain increments until fracture. Immediately after each load-unload cycle, the volume fraction and

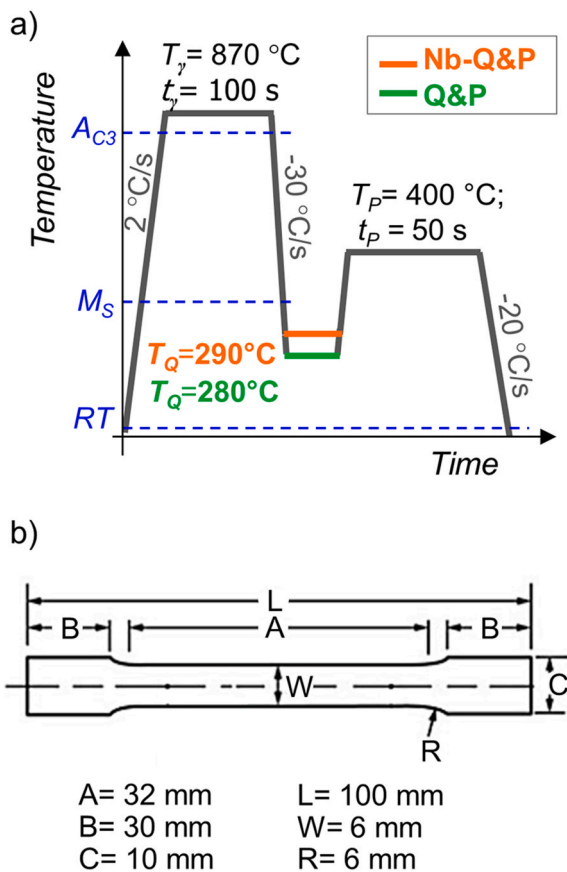


Fig. 3. (a) Schematics of the Q&P thermal cycles, where quenching temperatures of 280 $^\circ\text{C}$ and 300 $^\circ\text{C}$ were used for Q&P and Nb-Q&P, respectively; (b) Geometry of tensile specimens.

lattice parameter of the austenite were measured by XRD in order to study their evolution with the strain. The XRD measurements were done at the center of the specimens' gauge length (see set-up in Fig. 3c). For this purpose, one of the longitudinal sides of the tensile specimens was ground and polished down to 1 μm previous to testing.

In this case, peak fitting was used using two Pseudo-Voigt functions assuming Co $\text{K}\alpha_1 + \text{K}\alpha_2$ incident wavelength (Co $\text{K}\alpha_1 = 1.78897$ Å, $\text{K}\alpha_2 = 1.79285$ Å; $\text{K}\alpha_2$ area = 0.49 of $\text{K}\alpha_1$ area). The austenite {111} and ferrite {110} peaks were fitted together due to overlapping, as well as the austenite {222} and ferrite {220} peaks.

4. Results

4.1. Microstructural characterization

Fig. 4 shows SEM micrographs of the Q&P and Nb-Q&P steels. The primary martensite (M1) is the major phase and exhibits, what most likely are, transitional carbides formed during the partitioning stage at 400 °C [41]. XRD scans did not show carbide precipitation, though, which is probably due to the low volume fraction. The RA phase, revealed as the bright phase in the SEM, is present in blocks and films. The block-type RA exhibits a polygonal shape and is mainly located at prior austenite grain boundaries and martensite packet/block interface edges and corners. RA films of about 200 nm in thickness are observed in between the blocks and laths of martensite.

The volume fraction of RA and its carbon content (x_c^{RA}) were determined by XRD analyses. The carbon content of primary martensite (x_c^{M1}) was obtained by mass balance as $X_c^{\text{Steel}} = \sum_i f_i x_c^i$, where $i = \text{M1}$ and RA,

and X_c^{Steel} is the carbon content of the steel. Table 1 summarizes the volume fractions (f) and carbon content (x_c) of the constituent phases (M1 and RA) of the investigated Q&P steels, and the average grain size (d) and PAGS, as characterized in a previous work [36]. It is observed that x_c^{RA} of the Nb-Q&P is higher than that of the Q&P steel, in spite of the slightly higher RA volume fraction. Consequently, x_c^{M1} is lower in Nb-Q&P than in Q&P.

4.1.1. Electron backscatter diffraction

EBSD was used to characterize the crystallographic orientations, grain size and spatial distribution of the Q&P phases. Fig. 5 shows, from left to right, the Inverse Pole Figure (IPF) maps of the martensite (BCC phase) with outlined grain boundaries with misorientations of 10° or larger, the IPF maps of the retained austenite (FCC phase) in overlay with the Image Quality (IQ) map and the Orientation Distribution Function (ODF) maps of austenite and martensite for the $\varphi_2 = 45^\circ$ section of the Euler space obtained for Q&P (Fig. 5a) and Nb-Q&P (Fig. 5b).

Table 1

Volume fractions (f), carbon content (x_c), average grain size (d) of the Q&P constituent phases M1 and RA of the investigated steels and PAGS [36]. The uncertainty represents the maximum error in each case.

	f_{M1}	f_{RA}	x_c^{M1} (wt. %)	x_c^{RA} (wt. %)	PAGS (μm)	d_{M1} (μm)	d_{RA} (μm)
Q&P	0.88	0.12	0.09	1.03	8	3.50	0.40
Nb-Q&P	0.86	0.14	0.06	1.06	6	2.70	0.52
Uncertainty (\pm)	0.01	0.01	0.02	0.02	1	0.20	0.03

Spatial distribution of Q&P phases: The FCC-IPF maps show a quite homogeneous spatial distribution of the RA grains (spotted as the colored areas). RA grains sharing the same crystallographic orientation are usually distributed within the same region, since they belong to the same prior austenite grain [17]. The film-type RA, of about 100 nm or lower in thickness (Fig. 4b), cannot be observed by EBSD as the film thickness is lower than the detection limit of 200–250 nm, due to the step size (50 nm) and clean-up procedures involved in EBSD data post-processing. Therefore, mainly information of the block-type RA is provided by EBSD characterization.

Grain size of Q&P phases: The smaller PAGS of Nb-Q&P (6.0 μm) with respect to the Q&P steel (8.4 μm) displayed in Table 1 can be attributed to the nanoprecipitation of NbC. The Nb micro-addition also causes a refinement of d_{M1} from 3.50 μm to 2.70 μm (BCC-IPF maps of Fig. 5). The average RA grain size increases slightly from 0.40 μm (for Q&P) to 0.52 μm (for Nb-Q&P). Given the underrepresentation of film-RA grains by EBSD, the value of d_{RA} mainly represents the block-like RA grains.

Texture of Q&P phases: Although rather low for both steels, the martensite and austenite ODFs in Fig. 5 exhibit a slightly higher overall intensity ratio in presence of Nb. For martensite, gamma- and alpha-fibers are recognized in both steels. The maximum intensity in the martensitic texture is in the vicinity of the {554}<225> component, followed by the rotated cube. Further texture analysis details of the studied microstructures is presented in a previous work of the authors [9].

4.1.2. Transmission Electron Microscopy

TEM was used to characterize the nature and the size of the nanoprecipitates present in the Nb-containing steel and their possible influence on carbon consumption. Fig. 6 displays bright-field TEM micrographs of the Nb-Q&P steel. Fig. 6a gives an overview of the tempered martensite lath structure. The zoomed-in micrograph in Fig. 6b shows spherical carbides of two different sizes: large particles with a size of about 10 nm (labelled from 1 to 3) and small particles with size of 3.5 nm (4 and 5). Fig. 6c shows a high-magnification micrograph of particle

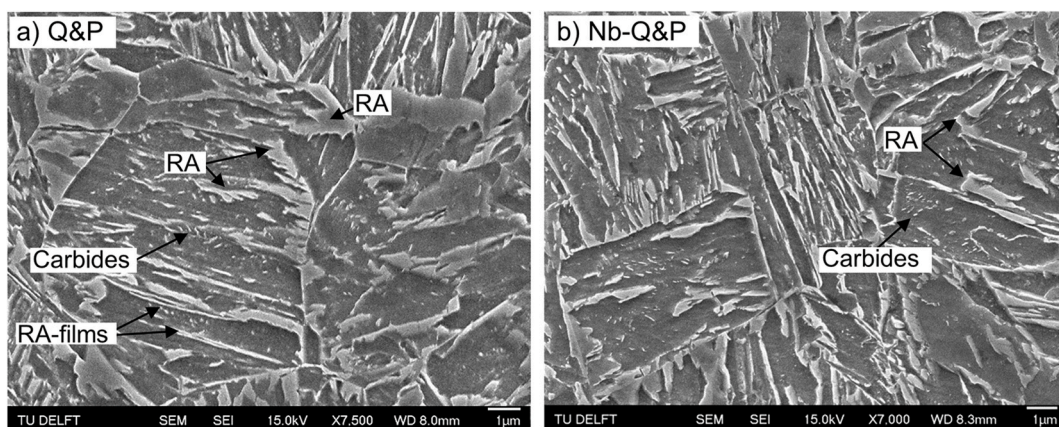


Fig. 4. SEM micrographs of the Q&P (a) and Nb-Q&P (b) steels. The blocks of retained austenite (RA), RA-films and carbides within the blocks of M1 are indicated by arrows.

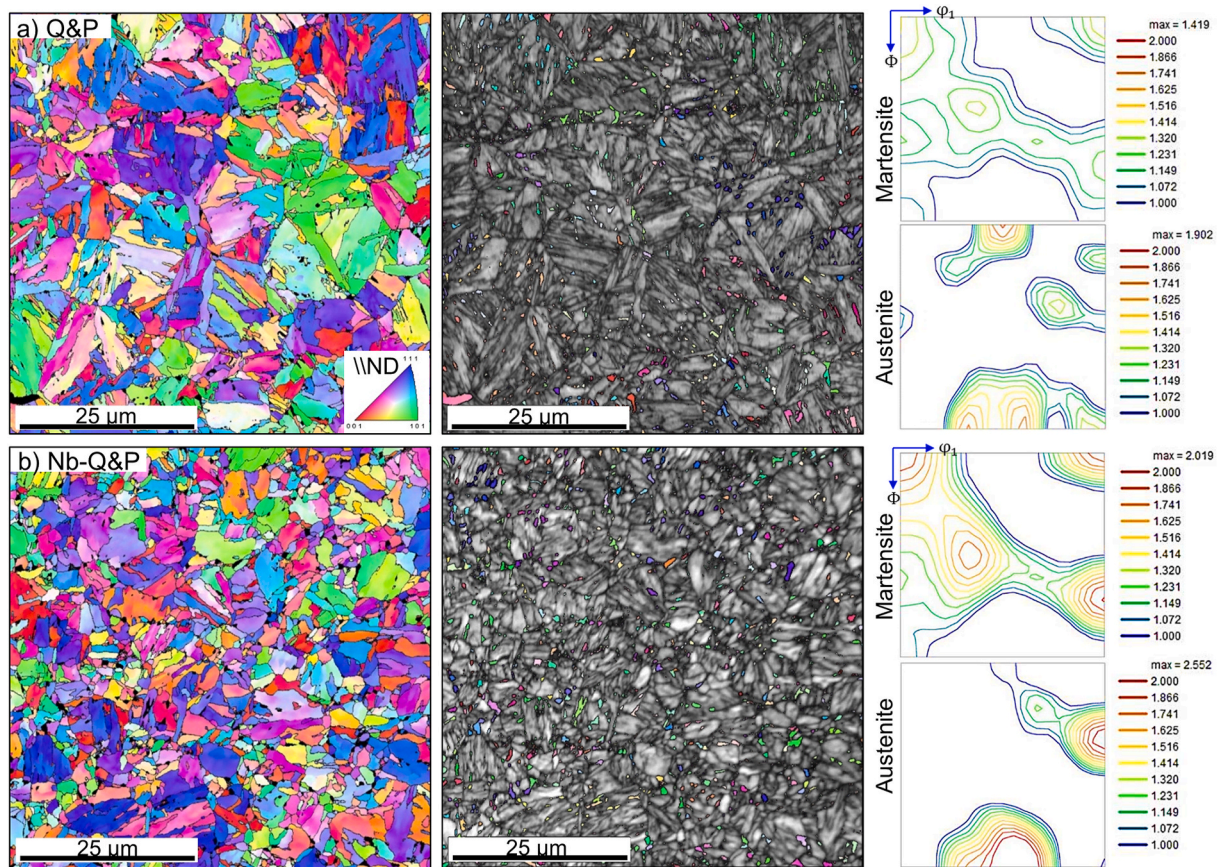


Fig. 5. IPF maps of the BCC (left) and FCC (center) phases of (a) the Q&P steel and (b) the Nb-Q&P steel. Boundaries with a misorientation of 10° or larger are outlined in black in the BCC-IPF maps. The image quality (IQ) map of the BCC phase is displayed in overlay with the FCC-IPF map. The right column displays the Orientation Distribution Functions (ODF) of martensite and austenite in the $\varphi_2 = 45^\circ$ section of the Euler space.

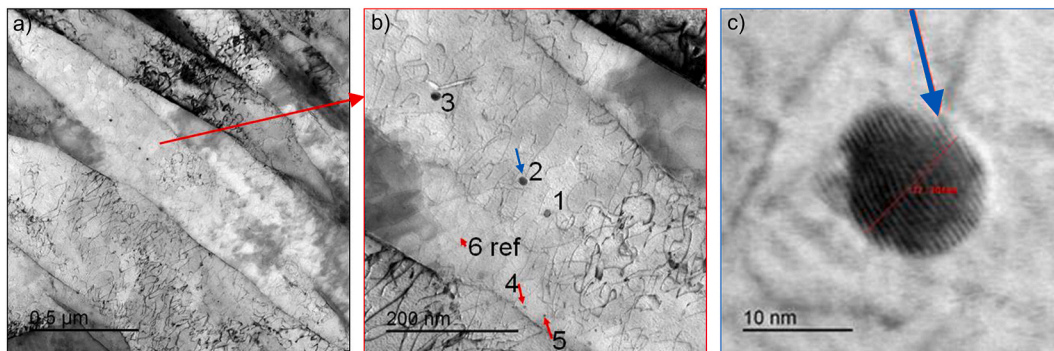


Fig. 6. Bright-field TEM micrographs of the Nb-Q&P steel: (a) overview of the martensitic lath structure; (b) zoomed-in image of a martensite lath, where spherical carbides are pointed by arrows. The numbers indicate the precipitates where TEM-EDX microanalysis was done; (c) detail of nanometer NbC precipitate number 2.

number 2. Table 2 summarizes the compositional energy-dispersive X-ray spectroscopy (EDS) microanalysis results for different particles and

Table 2
TEM-EDS microanalysis results (in wt. %, with balancing Fe) performed on different nanometer particles and the matrix (locations pointed in Fig. 6b).

Location	Size	Nb	Cr	Si	Mn	Ti
1	10.70	10.01	0.54	0.81	1.63	0.28
2	11.00	12.67	0.43	0.69	1.17	0.44
3	13.30	11.54	0.27	0.39	1.60	0.62
4	3.50	3.41	0.54	0.96	1.94	0.22
5	3.50	3.64	0.61	0.65	2.29	0.10
6 (Matrix)	—	0.00	0.71	1.18	2.03	0.10

the matrix. All particles are rich in Nb and are concluded to be of the type Nb(C,N), in agreement with ThermoCalc (TCFE9) results. In contrast to the SEM evidence, no transitional carbides were observed in the volume analyzed by TEM. The apparent decrease of Nb concentration as the particle size decreases is attributed to the large EDS analysis volume compared to that of the particle itself, due to which the analysis includes a larger volume fraction of the matrix. The bimodal NbC size distribution might be related to their precipitation temperatures. According to the recrystallization modeling results under an industrial hot strip schedule presented in an earlier work for the Nb-containing steel [42], only about 36% of the total Nb content precipitates during hot rolling and coiling. This was in good agreement with the experimental results obtained by TEM replicas and inductively coupled plasma optical

emission spectroscopy (ICP-MS) on a laboratory reversing mill hot-rolled steel of the same composition [42]. The high temperature during hot rolling allows the precipitates to grow, whereas the Nb that remains in solid solution can precipitate during the austenitisation stage of the Q&P cycle in the form of smaller carbides. The compositional analysis of the matrix indicates that there is no Nb in solid solution in the final Q&P microstructures.

The influence of NbC precipitation on the carbon content in M1 is considered negligible according to the following reasoning. If the Nb content precipitated in the final Q&P microstructures is assumed to be between 36% and 100% (0.009–0.025 wt %) [42], the volume fraction of NbC in the microstructure must be in the range $f_{\text{NbC}} = 1.0\text{--}2.8 \times 10^{-4}$. The precipitation of the NbC phase consumes 11.4 wt % of carbon and, thereby, would decrease the carbon content in M1 by 0.001–0.003 wt% for a 36%–100% of Nb precipitated. These are very small values compared to the overall carbon content in M1 (0.06–0.09 wt %, Table 1), which can be considered unaffected by NbC precipitation for the micro-addition of 0.025 wt % Nb.

4.2. Mechanical characterization

Fig. 7a shows the engineering stress–strain curves ($\sigma_e - \epsilon_e$) obtained by uniaxial tensile tests for both steels. The inset displays the tensile properties, where $YS_{0.2}$ and UTS stand for the 0.2% offset yield strength and ultimate tensile strength, and ϵ_{un} and ϵ_t represent the uniform and total strain, respectively. It is observed that the micro-addition of Nb significantly reduces the yield strength and increases the UTS of the Nb-Q&P steel with respect to the Q&P steel. Besides, the higher UTS in Nb-Q&P is accompanied by a higher uniform and total strain. Both steels exhibit a significant strain localization post-uniform strain, indicated by the difference between ϵ_{un} and ϵ_t .

Fig. 7b presents the true stress-strain curves, $\sigma_T - \epsilon_T$, (solid lines) and the work hardening rate, $\theta = \partial\sigma_T/\partial\epsilon_T$ (dashed lines), against the true strain. The volume fraction of RA (f_{RA}) measured by XRD after each load-unload cycle is represented by data points. From yielding onwards, the Nb-Q&P steel has a higher θ than the Q&P steel, particularly in the range of $\epsilon_T = 0.01\text{--}0.04$. In this early uniform deformation range, θ decreases steeply after yielding, and about 35% of the RA transforms into mechanically-induced martensite (α'_{mech}). From $\epsilon_T = 0.04$ to about 0.08, there is a plateau and θ decreases slowly and in a similar fashion for both steels until necking. In this later regime, an additional 15% of the RA transforms into α'_{mech} . The evolution of f_{RA} with the strain is very similar for both Q&P steels. About 50% of the total RA volume fraction remains untransformed until ϵ_{un} . The stress-strain curves reach Considère's criterion at $\theta = \sigma_T$. Once the localized plastic deformation begins, at the necked region, further transformation is triggered. Very low volume fractions of RA were measured near the necked region (f_{RA}^F in Fig. 7b), where local deformations of 42% (Q&P) and 39% (Nb-Q&P) were measured based on area reduction. In Fig. 7c, the work hardening rate has been represented against true strain on a logarithmic scale to magnify the behavior at low strains and at low θ . The Q&P steel exhibits a higher θ only for very low strains ($\epsilon_T < 5 \cdot 10^{-3}$).

5. Discussion

5.1. Influence of Nb microaddition on the Q&P microstructure and mechanical properties

According to equilibrium calculations performed with ThermoCalc software (TCFE9), the formation of the NbC phase takes place below 1157 °C in the austenite phase. Therefore, the NbC precipitates formed during hot rolling do not dissolve during the Q&P cycle, acting as obstacles against the austenite grain growth during the austenitisation stage and, in turn, affecting the further evolution of the Q&P constituent phases. As shown by Table 1, the micro-addition of Nb causes the

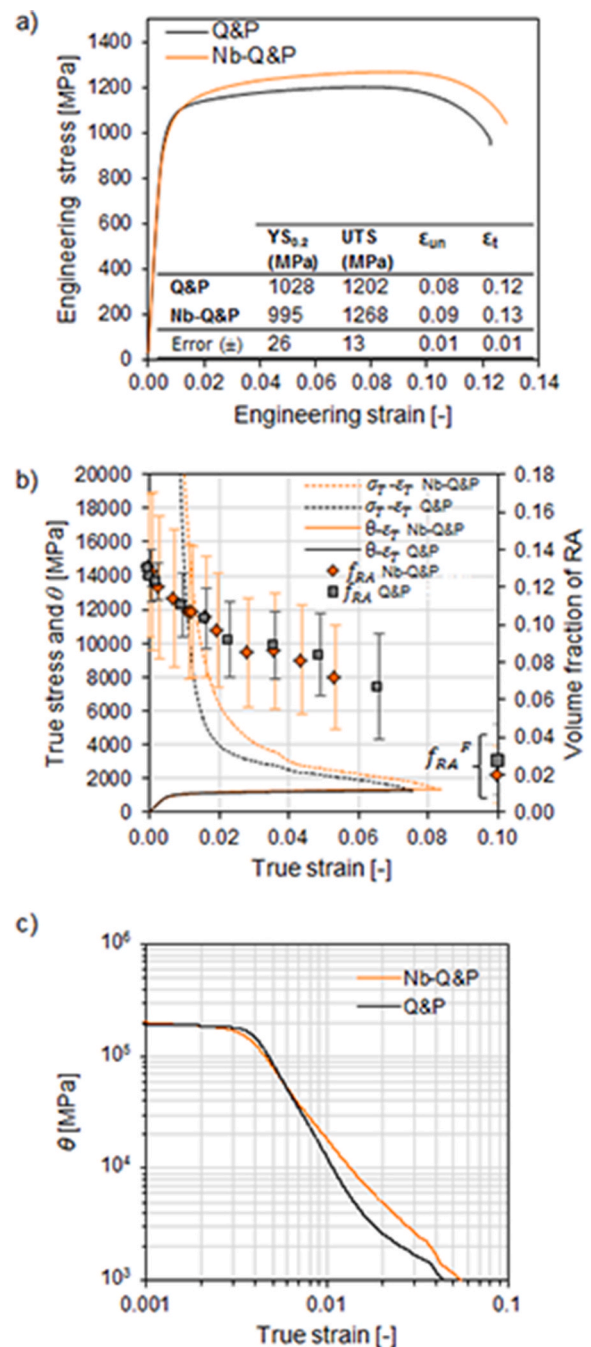


Fig. 7. (a) Engineering stress-strain curves and tensile properties of Q&P and Nb-Q&P, where the 0.2% offset yield strength ($YS_{0.2}$), ultimate tensile strength (UTS) and uniform and total elongations (ϵ_{un} and ϵ_t) are noted. The error refers to the maximum standard deviation. (b) True stress, work hardening rate (θ) and volume fraction of RA (data points) against true strain. The volume fraction of RA measured at the necked region after fracture is indicated as f_{RA}^F . (c) θ against true strain on a logarithmic scale.

refinement of the martensite structure and results in a higher carbon content in the RA, with respect to the Q&P steel (Table 1), according to the following reasoning. The martensite block size depends directly on the prior austenite grain size (PAGS) from which it forms. In a recent study of the authors on similar Q&P microstructures [20], it was observed that the PAGS refinement down to 6 μm leads to smaller and more globular martensite blocks and to a more homogeneous and finer spatial distribution of the untransformed austenite at the quenching temperature. Carbon-redistribution simulations using the DICTRA

module of ThermoCalc software revealed that such fine martensite block size and austenite spatial distribution makes the carbon partitioning process more efficient than that of α'/γ microstructures formed from coarser prior austenite. This explains the higher RA carbon content in the Nb-Q&P steel, given the fact the Nb micro-addition in the Nb-Q&P steel induces a smaller PAGS than that of the Q&P steel.

The final Nb-Q&P microstructure exhibits improved tensile strength and elongation compared to the non-microalloyed Q&P steel, which is attributed to the increased work hardening rate over the whole plastic deformation range (Fig. 7b). It is striking though, the lower yield strength obtained in the presence of Nb (Fig. 7a), despite its finer martensite structure, additional NbC nano-precipitation and higher RA carbon content. The underlying microstructural reason responsible for the yield strength of the investigated steels ($\sigma_{YS}^{Q\&P}$), can be clarified using a composite law:

$$\sigma_{YS}^{Q\&P} = \sum_i \sigma_{ys}^i \cdot f^i \quad 1$$

where σ_{ys}^i and f^i are the yield stress and volume fraction of phase i ($i = M1, RA$), respectively. Although the empirical formulae used to describe the microstructural contributions to the yield strength are widely accepted, their validation is limited by the ambiguous determination of the yield strength in multiphase steels, the experimental accuracy of the dislocation density or the complex strengthening role of carbon through solid solution and precipitation. Nevertheless, such models provide valid estimations of the M1 and RA yield strengths, with which the role of carbon in the primary martensite can be analyzed.

5.1.1. Retained austenite strength (σ_{ys}^{RA})

The yield strength of the RA depends on the alloying elements in solid solution and the grain size [7]:

$$\sigma_{ys}^{RA} = 15.4 \left(4.4 + 23x_C + 1.3x_{Si} + 0.24x_{Cr} + 32x_N + 0.94x_{Mo} + \frac{0.46}{\sqrt{d_{RA}}} \right) \quad 2$$

where the concentration of alloying elements is in wt. % and the grain size (d_{RA}), in millimeter. Using the data in Table 1 and the experimental $YS_{0.2}$, Equation (2) and Equation 1 render the absolute (σ_{ys}^i) and fraction-weighted ($\sigma_{ys}^i \cdot f$) contributions of RA and M1 to the yield strength for

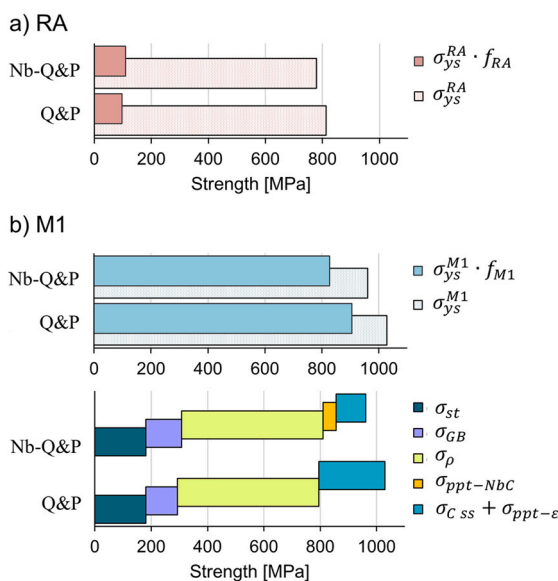


Fig. 8. Strengthening contributions to the Nb-Q&P and Q&P steels of (a) retained austenite and (b) primary martensite. The M1 total strengthening is broken down into the different microstructure contributions.

each steel, represented in Fig. 8a and b, respectively. The σ_{ys}^{RA} value in Nb-Q&P (780 MPa) is lower than that in the Q&P (813 MPa), indicating that the slightly higher RA carbon content in Nb-Q&P is counteracted by its somewhat larger grain size. Nevertheless, the slightly higher RA volume fraction in Nb-Q&P makes the contribution of its RA to the overall yield strength larger. In turn, the yield strength of M1 in Q&P is higher.

5.1.2. Primary martensite strength (σ_{ys}^{M1})

The strength of primary martensite (σ_{ys}^{M1}) can be described as:

$$\sigma_{ys}^{M1} = \sigma_C + \sum \sigma_j \quad 3$$

where the term $\sum \sigma_j$ accounts for the lattice friction stress for pure Fe (σ_0) and the strengthening contributions from substitutional alloying elements in solid solution (σ_{st}), forest dislocation (σ_{ρ}) and grain boundaries in the martensite sub-structure (σ_{GB}) [32]. Table 3 displays the equations that approximate these strengthening contributions. The role of carbon is taken into account in a separate term (σ_C), which includes solid solution ($\sigma_{C ss}$) and the precipitation strengthening from epsilon ($\sigma_{ppt-\epsilon}$) and Nb carbides ($\sigma_{ppt-NbC}$):

$$\sigma_C = \sigma_{C ss} + \sigma_{ppt-\epsilon} + \sigma_{ppt-NbC} \quad 4$$

To find σ_C , Equation 1 and Equation (3) are combined as:

$$\sigma_C = \left[\frac{\sigma_{YS}^{Q\&P} - \sigma_{ys}^{RA}}{f_{M1}} \right] - \sigma_{ys}^{RA} - \sum \sigma_j \quad 5$$

where $\sigma_{YS}^{Q\&P}$ is the experimental $YS_{0.2}$ (Fig. 7a), and σ_{ys}^{RA} and σ_j are theoretically calculated:

The **solid solution strengthening of substitutional alloying elements**, σ_{st} , is determined substituting the empirical data in Table 4 [43, 44] in Equation 6, with $\Delta\sigma^i$ the strength increment in MPa per 1 wt % of alloying element j . Given the small atomic misfit between the Cr and Fe atomic volumes and the marginal Nb content expected in solid solution (Table 2) [45], the effects of Cr and Nb are neglected. This results in the same influence of substitutional elements for both steels ($\sigma_{st ss} = 181$ MPa).

The **grain boundary strengthening**, σ_{GB} , (Equation 7) depends on the Hall-Petch coefficient, for martensite microstructures ($k_{HP} = 210 \text{ MPa}(\mu\text{m})^{1/2}$), and on the martensite block size (d_{M1}), which is considered the effective strengthening martensite subunit [32]. The calculation reveals that the martensite refinement in the Nb-Q&P steel only provides an additional strength of about 15 MPa with respect to the Q&P steel, for which $\sigma_{GB} = 112$ MPa.

The **forest dislocation strengthening**, σ_{ρ} , described by Equation 8, depends on the dislocation density (ρ), the shear modulus $G = 76$ GPa, for lath-structured martensite [48], the Burgers vector $b = 2.48 \times 10^{-10}$ m, the Taylor factor for martensite $M = 2.75$ [49] and $\alpha = 0.25$ [48]. By means of XRD, dislocation densities of $1.5 \times 10^{15} \text{ m}^{-2}$ have been estimated in primary martensite after partitioning at 400 °C for 50 s in similar Q&P steel compositions [15]. Similar values are inferred from the work of Kennett et al. [50] in low carbon, Nb-Ti microalloyed tempered martensite. Kennett et al. also observed that dislocation

Table 3
Strengthening mechanisms influencing the yield stress

Strengthening mechanism	Equation	Ref.
Solid solution	$\sigma_{st} = \sum_j \Delta\sigma \cdot x_j$	Equation 6 [43]
Grain boundaries	$\sigma_{GB} = k_{HP} \cdot d_{M1}^{-1/2}$	Equation 7 [32]
Forest dislocation	$\sigma_{\rho} = M\alpha G b \sqrt{\rho}$	Equation 8 [46]
Precipitation	$\sigma_{ppt} = \left(\frac{0.538Gb\sqrt{f_{ppt}}}{d_{ppt}} \right) \ln\left(\frac{d_{ppt}}{2b}\right)$	Equation 9 [47]

Table 4

Solid solution strengthening coefficients in MPa per 1 wt % of alloying elements in BCC Fe [43,44].

Element (j)	Si	Mn	Cu	Mo	C
$\Delta\sigma^j$ (MPa)/wt. %	83	32	39	11	4620

recovery due to tempering is insensitive to the Nb content in solid solution (for values of 0.003–0.021 wt % Nb). Therefore, a possible influence of Nb on the tempering degree of M1 and, thus its dislocation density, can be neglected and a value of $\rho = 1.5 \times 10^{15} \text{ m}^{-2}$ can be adopted as representative in both steels. Then, the strengthening contribution from the dislocation forest results in about 500 MPa.

The **carbon strengthening contribution**, σ_C , in M1 is found to be about 80 MPa lower in presence of Nb by Equation (5). As explained in Section 4.1.2 and previous work [42], the Nb content precipitated is expected to be between 36% and 100% of the nominal content, i.e. 0.009–0.025 wt % Nb. Considering these limits and the average carbide diameter of 8.5 nm measured by TEM (Fig. 6), Equation 9 renders lower and upper values of $\sigma_{ppt-NbC} = 34\text{--}57$ MPa, the mean value (46 MPa) being indicated by the orange bar in Fig. 8b. Then, the remaining contribution in Nb-Q&P (105 MPa) and in Q&P (234 MPa) can be attributed to the lattice friction stress for pure Fe ($\sigma_0 = 54$ MPa) and to $(\sigma_{C\text{ ss}} + \sigma_{ppt-\epsilon})$. Equation 6 and Equation 9 can be combined to find the theoretical $\sigma_{C\text{ ss}} + \sigma_{ppt-\epsilon}$ combination that fulfils the strengthening contribution of: 180 MPa (Q&P) and 51 MPa (Nb-Q&P), by assuming that ϵ -carbides (Fe_2C) have an average equivalent diameter of about 106 nm [51] and considering the M1 carbon content for each steel (Table 1) and a carbon solid solution strengthening of 4620 MPa/wt.% C [43]. The results, summarized in Table 5, show that most of the carbon content in M1 should be precipitated, with $f_{ppt-\epsilon} < 0.01$, and consequently $\sigma_{C\text{ ss}}$ is marginal, especially for Nb-Q&P. This estimation agrees well with experimental quantification of volume fractions of epsilon carbides in similar Q&P steels (of 0.01 or lower) [7,15]; however, experimental measurements by Atom Probe Tomography quantify the carbon content in solid solution in M1 as around 0.05 wt % C [7]. This suggests that the solute carbon content in M1 in the investigated steels might be higher than that estimated in Table 5. In such a case, the strengthening coefficient for solute carbon used in this work would be overestimated. According to the M1 strength reduction of 80 MPa in presence of Nb and a difference in 0.03 wt % C in the total M1 carbon content, a strengthening coefficient of 2667 MPa/wt. % C is deduced.

In summary, this microstructure-based analysis of the macroscopic yield strength suggests that the lower $\text{YS}_{0.02}$ of Nb-Q&P with respect to Q&P stems from a lower overall carbon content in M1, which counteracts the strengthening influence from the refined martensite and the NbC nanoprecipitation. Since carbon consumption by NbC formation is marginal, the lower M1 carbon content in Nb-Q&P is attributed to the more efficient carbon partitioning process and the thus-obtained higher total carbon content in RA and larger RA fraction.

5.2. Effect of carbon in M1 on the work hardening of the Q&P steels

The proposed approach (Section 2) is applied to analyze the microstructure features controlling the work hardening of the individual Q&P phases and the overall microstructure. This section is organized as follows: first, the phase parameters are identified and, then, the plastic

Table 5

Estimated precipitated fractions and carbon balance between precipitates ($x_{C\text{ ppt-}\epsilon/\text{-NbC}}$) and solid solution ($x_{C\text{ ss}}$) in primary martensite, with $\sigma_{ppt-\epsilon/\text{-NbC}}$ and $\sigma_{C\text{ ss}}$ the correspond strengthening contributions, and σ_0 the friction coefficient for pure Fe.

	$f_{ppt-NbC}$	$f_{ppt-\epsilon}$	$x_{C\text{ ppt-NbC}}$ (wt. %)	$x_{C\text{ ppt-\epsilon}}$ (wt. %)	$x_{C\text{ ss}}$ (wt. %)	σ_0 (MPa)	$\sigma_{ppt-NbC}$ (MPa)	$\sigma_{ppt-\epsilon}$ (MPa)	$\sigma_{C\text{ ss}}$ (MPa)
Q&P	–	0.007	–	0.060	0.030	54	–	42	138
Nb-Q&P	1.9×10^{-4}	0.007	0.002	0.058	0.002	54	46	41	10

deformation behavior of the individual phases is analyzed combining theoretical knowledge on hardening with crystal plasticity simulations using single-phase RVEs of M1 and RA. Finally, the M1/RA composite plastic deformation response is analyzed by comparison of the experimental response to that obtained from the simulations of mechanically-stable M1/RA RVEs.

5.2.1. Identification of material parameters

According to the phenomenological Crystal Plasticity law employed in this study, the initial critical slip resistance ($\tau_{c,0}$) represents the stress at which dislocations start to move, the saturation slip resistance (τ_{sat}) can be interpreted as the stress at which moving dislocations of active slip systems get completely pinned due to hardening and further dislocation glide is prevented. The asymptotic evolution of $\tau_{c,0}$ into τ_{sat} is described by the fitting hardening parameters h_0 and a . A theoretical basis for the parameter identification of the RA and M1 phases is proposed.

Retained austenite: The initial slip resistance ($\tau_{c,0}$) can be calculated based on the work of Gil-Sevillano [52], where the critical resolved shear stress of a single crystal, τ , and the macroscopic yield strength, σ , are related through a misorientation factor (M): $\sigma = M \cdot \tau$. Equation (2) gives the theoretical value of σ for RA (Section 5.1.1) and $M = 3.06$ is adopted for random texture [53]. Since, in this methodology, the austenite is described as a mechanically-stable phase, τ_{sat} and the hardening parameters are adopted from the description of the stable austenite films that exist in between the laths in martensitic microstructures provided by Maresca et al. [54] leading to: $\tau_{sat} = 1.3 \cdot \tau_{c,0}$, with $a = 1.5$ and $h_0 = 250$.

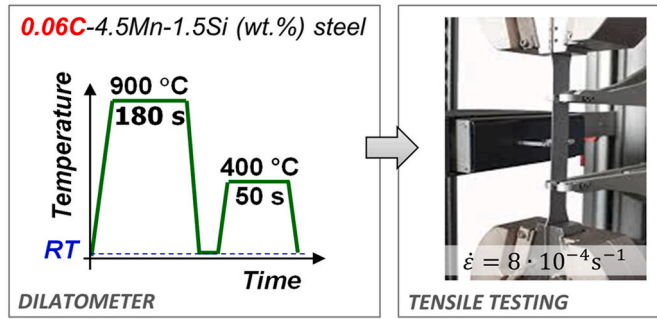
Primary martensite: The methodology consists of various steps and is schematized in Fig. 9.

- Experimental step:** A steel of a composition comparable to that of M1 in the final Q&P microstructures, particularly in terms of carbon content, is selected and thermally processed to match the tempering state. The designed low-carbon and tempered martensite is then mechanically tested. Based on the carbon content of primary martensite in Q&P-processed steels (Table 1), a 0.06C-4.5Mn-1.6Si (wt. %) steel was selected. Tensile dilatometry specimens of 10 mm in gauge length were machined and heat treated to create a tempered fully martensitic microstructure in a Bähr DIL 805 A/D dilatometer under vacuum, using the same thermal parameters as in the Q&P partitioning stage. Then, uniaxial tensile tests were carried out in an Instron 5500 machine, at a strain rate of $8 \cdot 10^{-4} \text{ s}^{-1}$, using a contact extensometer of 7.8 mm in initial span.
- Numerical step:** A martensite RVE is created with 5000 grains, where each grain represents a martensite block with average representative crystallographic orientations (Fig. 9b). The RVE is discretized in 64^3 voxels and subjected to uniaxial virtual testing along RD, at the experimental strain rate, and using initial parameters based on ref. [54] and Gil-Sevillano's expression, $\sigma = M \cdot \tau$ [52], with $M = 2.75$, as representative of martensite texture. Then, the simulated overall response is fitted to the experimental true stress-strain curve by adjusting $\tau_{c,0}$, τ_{sat} and h_0 to minimize the sum of the squared differences:

$$\sum [\sigma(h_0, \tau_{c,0}, \tau_{sat}, \epsilon_T) - \sigma_T]^2 \quad 10$$

A) Experimental step:

Mechanical testing of designed tempered martensite



B) Numerical step:

DAMASK CP simulations and fitting

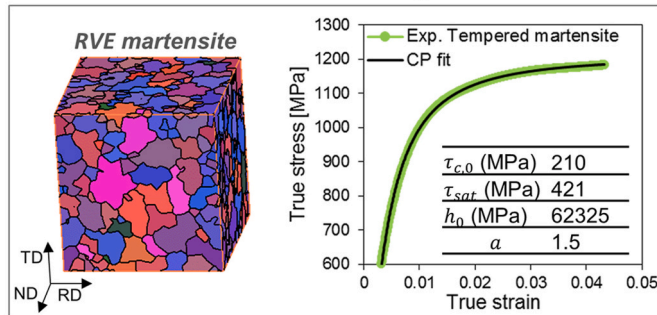


Fig. 9. Methodology to identify the phase parameters of primary martensite under uniaxial tensile deformation.

About 2–3 iterations of CP simulations and fitting are needed to reach stable parameter values. The experimental tensile curve and the identified CP parameters of the designed tempered martensite (0.06 wt % C) are shown in Fig. 9b.

C) *Scaling due to differences in carbon content*: The flow behavior of the M1 phase in Q&P, with 0.09 wt % C, is expected to scale up with respect to that of the designed tempered martensite, with 0.06 wt % C. The analysis performed in Section 5.1.2 yielded a carbon strengthening coefficient of $\Delta\sigma_C = 2667 \text{ MPa/wt. \% C}$, which translates into $\Delta\tau \approx 970 \text{ MPa/wt. \% C}$ using Gil-Sevilla's expression, $\Delta\sigma = M \cdot \Delta\tau$ [52], with $M = 2.75$. Therefore, $\tau_{c,0}$ and τ_{sat} are considered to increase by $\Delta\tau \approx 29 \text{ MPa}$ for Q&P with respect to Nb-Q&P. The hardening parameters are assumed to remain invariant for such small variations in carbon content. Table 6 summarizes the identified M1 and RA parameters. The

Table 6

Primary martensite and retained austenite parameters for CP simulations.

Phase parameter	Symbol	Primary martensite		Retained austenite	
		Q&P	Nb-Q&P	Q&P	Nb-Q&P
Elastic stiffness constants [GPa]	C_{11}	233.5		268.5	
	C_{12}	135.5		156	
	C_{44}	118		136	
Initial shear rate [s^{-1}]	$\dot{\gamma}_0$	0.01		0.01	
Strain rate sensitivity	n	20		20	
Initial critical slip resistance [MPa]	$\tau_{c,0}$	239	210	265	255
Saturation slip resistance [MPa]	τ_{sat}	450	421	340	326
Initial hardening parameter [MPa]	h_0	62325		250	
Hardening numerical value	a	1.5		1.5	

elastic stiffness constants and the initial shear rate ($\dot{\gamma}_0$) were adopted from the literature [54], and the strain rate sensitivity (n) is constant in this case, but not relevant, as strain rate effects are not studied.

5.2.2. Deformation behavior of the individual phases

Fig. 10 shows the single-phase RA and M1 RVEs and the corresponding simulated flow curves. The mechanically-stable retained austenite exhibits low hardening ability and owes the high strength to high average carbon content and the nanometer grain size, particularly in Q&P. The predicted RA strengths agree well with those observed through load partitioning analysis of *in-situ* monotonic tensile tests during HE-XRD by Hidalgo et al. in similar Q&P microstructures [16]. The simulated curves obtained for primary martensite agree well with experimental observations in tempered martensite with similar carbon contents [55]. Compared to the RA, yielding in M1 occurs at lower stresses and continuously, i.e. in wide elastic-plastic transition, as representative of martensitic microstructures [55,56].

The simulated macroscopic curves of individual phases point out the sensitivity of the crystal plasticity material parameters to the processing-dependent microstructure features, like carbon content. This is particularly relevant in the case of primary martensite, in Q&P-processed steels.

5.2.3. Martensite/austenite composites: the role of the TRIP effect

Fig. 11 shows the martensite/austenite RVEs representing the Q&P (a) and Nb-Q&P (b) microstructures and the corresponding experimental (solid line) and simulated (line with markers) stress-strain curves. As expected, the simulated curves of the mechanically-stable RVEs deviate considerably from the experimental ones. The experimental-numerical deviation, $\Delta\sigma^T$ (Exp-Sim), is obtained by subtraction of the simulated to the experimental curve (dashed line). For deformation levels of $\varepsilon_T \leq 0.02$, the formation of α'_{mech} along with the composite effect in real Q&P steels, i.e. presence of non-connected hard RA particles within M1, lead to a higher strength and work hardening rate compared to the mechanically-stable RVE response. For $\varepsilon_T > 0.02$ (shaded region), the strength increment, $\Delta\sigma^T$ (Exp-Sim), per strain increment ($\varepsilon_{i+1} - \varepsilon_i$) can be assumed to be proportional to the formation of the harder α'_{mech} from the retained austenite. Thus, it can be theoretically calculated as:

$$\sigma^T(\varepsilon_{i+1}) - \sigma^T(\varepsilon_i) = (\sigma'_{\alpha'_{mech}} - \sigma_{RA}) \cdot [f'_{\alpha'_{mech}}(\varepsilon_{i+1}) - f'_{\alpha'_{mech}}(\varepsilon_i)] \quad 11$$

where the right-hand side term represents the experimental increment in α'_{mech} volume fraction at each incremental strain, as measured from the consecutive load-unload tensile tests (Fig. 7b), and $(\sigma'_{\alpha'_{mech}} - \sigma_{RA})$ represents the flow stress difference between RA and the newly formed α'_{mech} , which is theoretically calculated: for σ_{RA} , the values in Fig. 8a are adopted, and $\sigma'_{\alpha'_{mech}}$ is based on the solid solution strengthening considering the steel's nominal composition (Table 4, Equation 6) and the inherited RA carbon content as: $\Delta\sigma_C = 3065x_C - 161 \text{ MPa}$ [44]. This yields average values of $\sigma'_{\alpha'_{mech}} = 2960 \text{ MPa}$ for Q&P, and $\sigma'_{\alpha'_{mech}} = 3052 \text{ MPa}$ for Nb-Q&P.

In order to examine the role of the primary martensite in the TRIP strengthening contribution, the theoretical predictions of $\Delta\sigma^T(\varepsilon)$ by Equation 12 are compared to the experimental-numerical deviation (Exp-Sim) in Fig. 12. The predicted $\Delta\sigma^T(\varepsilon)$ trends are quite similar for both steels' microstructures, owing to the comparable RA decomposition rates with the strain (Fig. 7b). An overestimation of $\Delta\sigma^T$ for $\varepsilon_T < 0.02$, and an underestimation for $\varepsilon_T \geq 0.04$, can be expected since an average RA carbon content is considered Equation (11), while the average carbon content in the untransformed RA is known to increase in a quite linear fashion as α'_{mech} forms [16]. The comparison of the predicted $\Delta\sigma^T(\varepsilon)$ with that obtained through the experimental-numerical mismatch in Fig. 11 (Exp-Sim) for $\varepsilon_T > 0.02$ reveals that, despite the

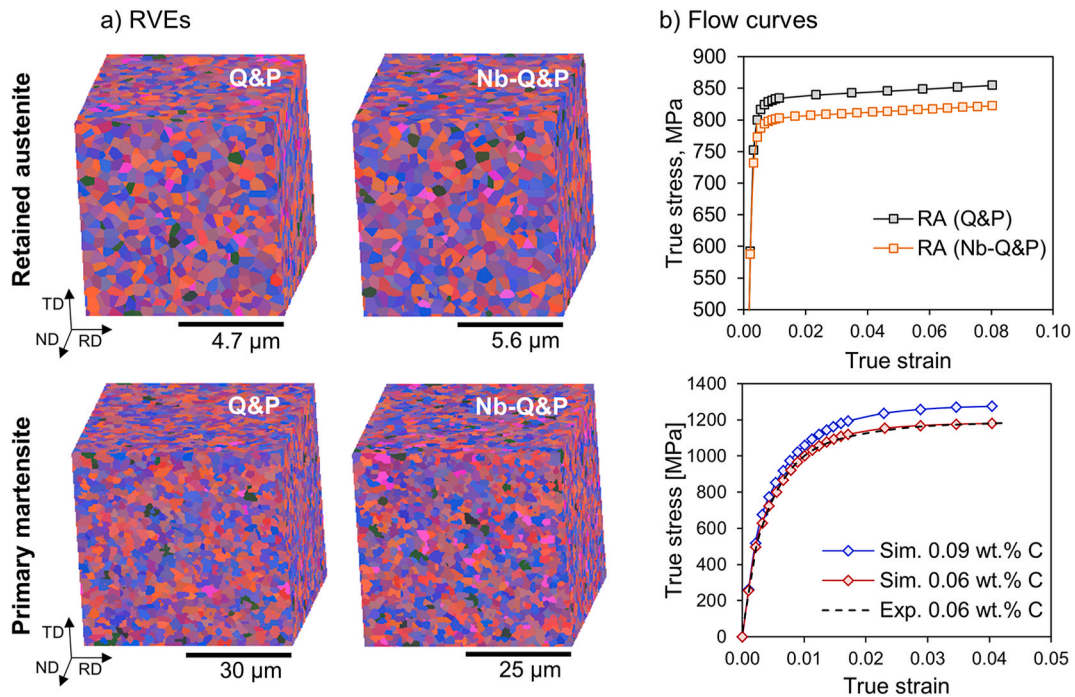


Fig. 10. a) RVEs of the individual phases: mechanically-stable retained austenite (upper row) and primary martensite (bottom row) and b) corresponding flow curves after virtual uniaxial testing using the phase parameters listed in Table 6.

similar martensite transformation kinetics, the TRIP strengthening contribution is larger in Nb-Q&P, and lower in Q&P, than predicted by Equation (11). This contribution ($\Delta\theta_{M1}$, highlighted as shaded areas in Fig. 12) might further enhance or partially counteract the strengthening contribution of the RA-to- α'_{mech} transformation, as shown for Nb-Q&P ($\Delta\theta_{M1} > 0$) and Q&P ($\Delta\theta_{M1} < 0$), respectively. Therefore, besides the RA being replaced by the harder α'_{mech} as the steel is strained, there is an additional strengthening contribution by the mechanical response of the surrounding M1, and the methodology presented in this study allows for its systematic evaluation.

The origin of this enhancement or shielding of the TRIP strengthening can be related to the carbon content and distribution in the primary martensite according to the following reasoning. The RA-to- α'_{mech} lattice transformation entails a volume expansion, whose magnitude depends on the RA carbon content and the local redistribution of the strain next to the M1/ α'_{mech} interface, i.e. dislocation multiplication in M1 to accommodate the plastic deformation. The dislocation multiplication in martensite is known to become more prominent as its carbon content in solid solution increases [57]. The analysis presented in Fig. 8 shows that, whereas the austenite strength in both microstructures is very similar, the martensite strength is lower in the presence of Nb. The theoretical evaluation of the carbon distribution suggests that most of the carbon content in M1 is precipitated as nanometer-sized and elongated ϵ -carbides, in Q&P, and as nanometer-sized and round-shaped NbC, in Nb-Q&P. The somewhat higher M1 carbon content in Q&P in the form of ϵ -carbides results in a higher work hardening rate in M1 at low strains during uniaxial loading (Fig. 7c), which further increases the M1 strength and thus the energy needed for dislocation multiplication. This, consequently, decreases the strengthening capacity of the TRIP effect at larger strains. In contrast, the lower carbon content of M1 in Nb-Q&P, mostly in the form of NbC nano-precipitates, appears to lead to a more sustained work hardening ability over the whole uniform deformation range, enhancing the overall strength-ductility values with respect to Q&P. The positive influence of nano-precipitates on the work hardening of martensite and on the overall ductility has been already highlighted in the literature. Raabe and co-authors [58] found the synergetic effect from intermetallic nano-precipitates, plus TRIP effect,

beneficial to increase significantly the ductility while maintaining the ultra-high strength in a maraging steel. Besides, Peng et al. [59] demonstrated by molecular dynamics simulations in copper that, at sufficiently high stress, nanoscale precipitates might act as dislocation sources and obstacles when the precipitate density, size and spacing is adequately designed. Similar self-hardening mechanisms to those proposed by Raabe and Peng might be acting in Nb-Q&P, resulting into enhanced strength-ductility balances.

The results presented in this section highlight that, in addition to the stabilization of maximum austenite volume fractions, the strength of the carbon-depleted martensite should be considered a key parameter for the design of Q&P steels with improved strength-ductility combinations. Further understanding is needed of how exactly the composition and the Q&P-processing-dependent microstructure parameters affect the strength and work hardening ability of the martensite.

6. Conclusions

The presented experimental-numerical method offers a quantitative and systematic means to examine the role of the martensite mechanical behavior, through its carbon content and distribution, in the strengthening contribution provided by the formation of mechanically-induced martensite (α'_{mech}) in Q&P-processed α'/γ microstructures.

The methodology rests on the generation of a 3D micro-mechanical model that allows to derive, by crystal plasticity simulations, the overall response of a mechanically-stable α'/γ virtual microstructure, or representative volume element (RVE). In combination with theoretical knowledge on hardening, the comparison between the experimental and simulated mechanical responses enables the quantification of the influence of the martensite carbon content and distribution on the overall strengthening resulting from: 1) the austenite being replaced by the α'_{mech} , and 2) the thus-induced work hardening in the martensite to accommodate the plastic deformation resulting from the lattice volume expansion associated to the martensitic transformation. The approach is applied to two low carbon Q&P-processed α'/γ microstructures of similar composition, one containing a Nb-microaddition and displaying improved strength-ductility values, even though both microstructures

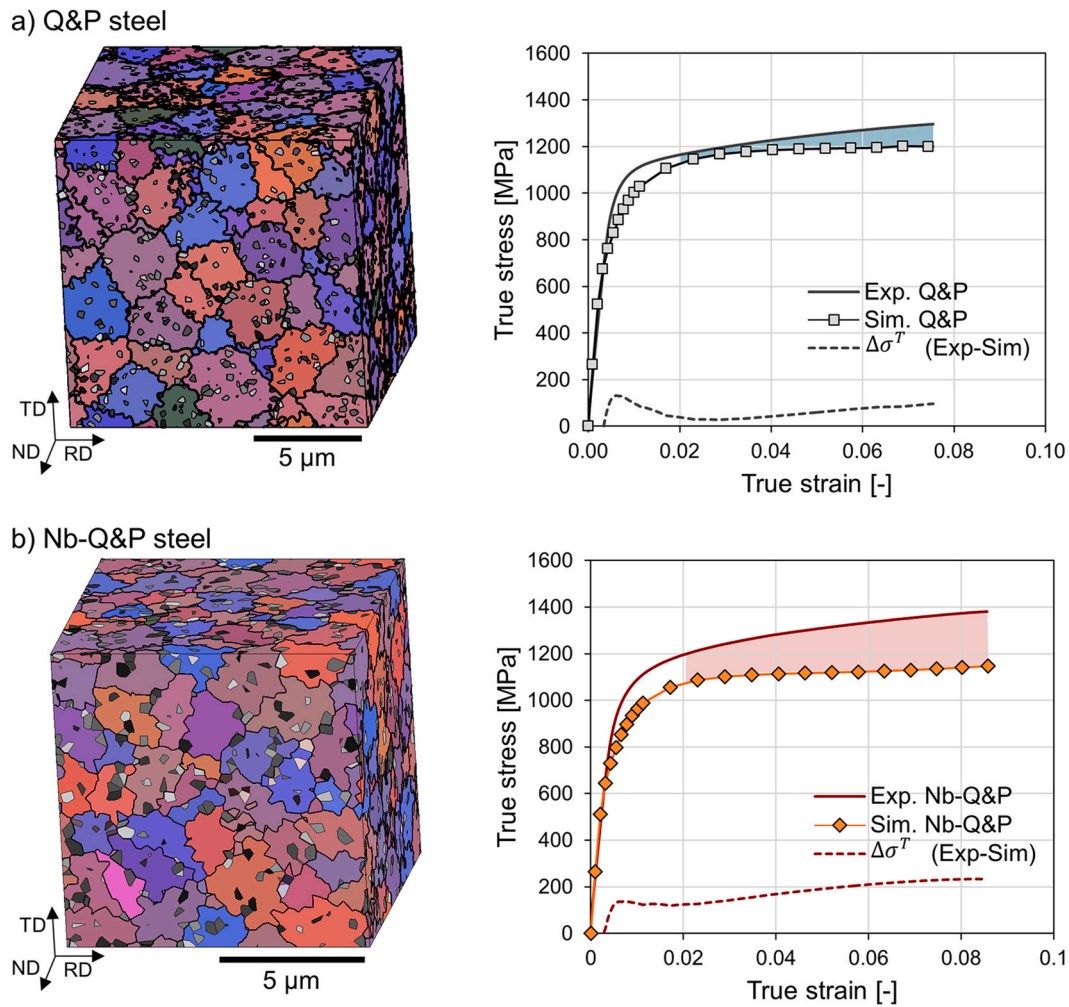


Fig. 11. RVEs of the M1/RA composites representing the investigated Q&P steels, where the small and large grains represent the RA and M1 phases, respectively, and corresponding experimental and simulated flow curves. The TRIP effect contribution corresponds to the mismatch between experiments and simulations.

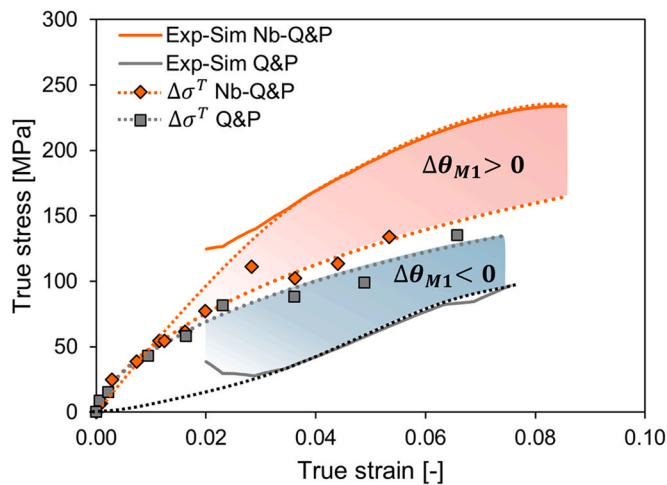


Fig. 12. Strength increment expected from the TRIP effect ($\Delta\sigma^T$) according to the experimentally measured volume fraction of α'_{mech} (data points) and strength increment obtained after comparing the experimental tensile tests with the simulations of the M1/RA composite RVEs (Exp-Sim).

exhibit similar initial volume fractions of austenite and α'_{mech} formation kinetics. The following conclusions are drawn:

- The mechanical response of the primary martensite (M1) might further enhance or partially counteract the strengthening contribution from the austenite-to-mechanically induced martensite transformation, depending on the strength and work hardening ability of the martensite. The mechanical behavior of M1 is sensitive to the carbon content and distribution evolved during the Q&P thermal cycle. In the investigated Q&P-processed α'/γ microstructures, the Nb microaddition results in a refined martensite structure of a lower carbon content (0.06 wt %), with respect to the non-microalloyed composition (0.09 wt % C). Theoretical calculations suggest that most of the carbon fraction in the primary martensite is precipitated as nanometer, round-shaped NbC particles.
- Contents of 0.09 wt% C in the primary martensite, mostly precipitated as nanometer, elongated ϵ -carbides, increase the martensite strength and work hardening rate at low strains. This, consequently, decreases the TRIP strengthening capacity of the steel at larger strains. In contrast, contents of 0.06 wt% C in M1, mostly precipitated as nanometer, round-shaped NbC, decrease the M1 strength and provides a more sustained work hardening rate over the whole uniform deformation range, enhancing the overall strength-ductility values of the steel.

The presented method will aid the microstructural design and

optimization of Q&P processed steels, and other advanced high-strength steels, by providing a deeper insight into the role of microstructural modifications in the intrinsic strength and work hardening ability of the individual phases and their mechanical interactions.

CRediT authorship contribution statement

Carola Celada-Casero: Conceptualization, Methodology, Investigation, Formal analysis, Visualization, Writing – original draft. **Florian Vercruyse:** Investigation, Formal analysis, Visualization, Writing – review & editing. **Bernd Linke:** Investigation, Formal analysis, Resources, Writing – review & editing. **Ali Smith:** Investigation, Formal analysis, Resources, Writing – review & editing. **Piet Kok:** Software, Resources, Investigation, Writing – review & editing. **Jilt Sietsma:** Conceptualization, Writing – review & editing, Project administration, Funding acquisition. **Maria Jesus Santofimia:** Conceptualization, Writing – review & editing, Project administration, Funding acquisition.

Declaration of competing interest

The authors declare that they have no known competing financial interests or personal relationships that could have appeared to influence the work reported in this paper.

Acknowledgments

The authors deeply acknowledge the support from the Research Fund for Coal and Steel for funding this research via the OptiQPap project, under the Contract RFCS-02-2015 (No. 709755). Richard Huizenga at the Department of Materials Science and Engineering of the Delft University of Technology is acknowledged for the X-ray analysis. C. Celada-Casero is grateful to W. Spanjer and F. Korver for their support with crystal plasticity simulations and generation of representative volume elements. The authors also express their gratitude to Dr. I. Sabirov, Professor R. Petrov, Professor P. Verleysen and Dr. R. Thiessen for the fruitful discussions during the development of the OptiQPap project.

References

- [1] D.K. Matlock, J.G. Speer, Springer London, London, 2009, pp. 185–205.
- [2] J.G. Speer, D.V. Edmonds, F.C. Rizzo, D.K. Matlock, *Curr. Opin. Solid State Mater. Sci.* 8 (2004) 219–237.
- [3] D.V. Edmonds, K. He, F.C. Rizzo, B.C. De Cooman, D.K. Matlock, J.G. Speer, *Mater. Sci. Eng., A* 438–440 (2006) 25–34.
- [4] I. de Diego-Calderón, M.J. Santofimia, J.M. Molina-Aldareguia, M.A. Monclús, I. Sabirov, *Mater. Sci. Eng., A* 611 (2014) 201–211.
- [5] J. Hidalgo, K.O. Findley, M.J. Santofimia, *Mater. Sci. Eng., A* 690 (2017) 337–347.
- [6] I. de Diego-Calderón, D. De Knijf, M.A. Monclús, J.M. Molina-Aldareguia, I. Sabirov, C. Föjer, R.H. Petrov, *Mater. Sci. Eng., A* 630 (2015) 27–35.
- [7] F. HajyAkbari, J. Sietsma, G. Miyamoto, N. Kamikawa, R.H. Petrov, T. Furuhashi, M.J. Santofimia, *Mater. Sci. Eng., A* 677 (2016) 505–514.
- [8] E.J. Seo, L. Cho, Y. Estrin, B.C. De Cooman, *Acta Mater.* 113 (2016) 124–139.
- [9] F. Vercruyse, C. Celada-Casero, B.M. Linke, P. Verleysen, R.H. Petrov, *Metals* 10 (2020) 22.
- [10] E. Jimenez-Melero, N.H. van Dijk, L. Zhao, J. Sietsma, S.E. Offerman, J.P. Wright, S. van der Zwaag, *Acta Mater.* 55 (2007) 6713–6723.
- [11] K.-i. Sugimoto, M. Misu, M. Kobayashi, H. Shirasawa, *ISIJ Int.* 33 (1993) 775–782.
- [12] P.J. Jacques, F. Delannay, J. Ladrière, *Metall. Mater. Trans.* 32 (2001) 2759–2768.
- [13] D. De Knijf, R. Petrov, C. Föjer, L.A.I. Kestens, *Mater. Sci. Eng., A* 615 (2014) 107–115.
- [14] J. Hidalgo, C. Celada-Casero, M.J. Santofimia, *Mater. Sci. Eng., A* 754 (2019) 766–777.
- [15] K.O. Findley, J. Hidalgo, R.M. Huizenga, M.J. Santofimia, *Mater. Des.* 117 (2017) 248–256.
- [16] J. Hidalgo, R.M. Huizenga, K.O. Findley, M.J. Santofimia, *Mater. Sci. Eng., A* 745 (2019) 185–194.
- [17] M.J. Santofimia, L. Zhao, R. Petrov, C. Kwakernaak, W.G. Sloof, J. Sietsma, *Acta Mater.* 59 (2011) 6059–6068.
- [18] F. HajyAkbari, J. Sietsma, G. Miyamoto, T. Furuhashi, M.J. Santofimia, *Acta Mater.* 104 (2016) 72–83.
- [19] S.Y.P. Allain, G. Geandier, J.C. Hell, M. Soler, F. Danoix, M. Gouné, *Scripta Mater.* 131 (2017) 15–18.
- [20] C. Celada-Casero, C. Kwakernaak, J. Sietsma, M.J. Santofimia, *Mater. Des.* (2019) 107847.
- [21] S. Ayenampudi, C. Celada-Casero, J. Sietsma, M.J. Santofimia, *Materialia* 8 (2019) 100492.
- [22] C. Celada-Casero, J. Sietsma, M.J. Santofimia, *Mater. Des.* (2019) 107625.
- [23] S. Yadegari, S. Turteltaub, A.S.J. Suiker, P.J.J. Kok, *Comput. Mater. Sci.* 84 (2014) 339–349.
- [24] P.J.J. Kok, W. Spanjer, H. Vegter, *KEM* 651–653 (2015) 975–980.
- [25] M. Amirmaleki, J. Samei, D.E. Green, I. van Riemsdijk, L. Stewart, *Mech. Mater.* 101 (2016) 27–39.
- [26] A. Ramazani, K. Mukherjee, H. Quade, U. Prah, W. Bleck, *Mater. Sci. Eng., A* 560 (2013) 129–139.
- [27] G. Anand, P. Dey, P.J.J. Kok, D. Chakraborty, P.P. Chattopadhyay, *Mater. Sci. Technol.* 30 (2014) 1086–1093.
- [28] C.C. Tasan, M. Diehl, D. Yan, C. Zambaldi, P. Shanthraj, F. Roters, D. Raabe, *Acta Mater.* 81 (2014) 386–400.
- [29] C.C. Tasan, J.P.M. Hoefnagels, M. Diehl, D. Yan, F. Roters, D. Raabe, *Int. J. Plast.* 63 (2014) 198–210.
- [30] C.C. Tasan, J.P.M. Hoefnagels, M.G.D. Geers, *Scripta Mater.* 62 (2010) 835–838.
- [31] T. Park, L.G. Hector, X. Hu, F. Abu-Farha, M.R. Fellingner, H. Kim, R. Esmailpour, F. Pourboghrat, *Int. J. Plast.* 120 (2019) 1–46.
- [32] S. Morito, H. Yoshida, T. Maki, X. Huang, *Mater. Sci. Eng., A* 438–440 (2006) 237–240.
- [33] F. Roters, M. Diehl, P. Shanthraj, P. Eisenlohr, C. Reuber, S.L. Wong, T. Maiti, A. Ebrahimi, T. Hochrainer, H.O. Fabritius, S. Nikolov, M. Friák, N. Fujita, N. Grilli, K.G.F. Janssens, N. Jia, P.J.J. Kok, D. Ma, F. Meier, E. Werner, M. Stricker, D. Weygand, D. Raabe, *Comput. Mater. Sci.* 158 (2019) 420–478.
- [34] S.L. Wong, M. Madivala, U. Prah, F. Roters, D. Raabe, *Acta Mater.* 118 (2016) 140–151.
- [35] P. Eisenlohr, M. Diehl, R.A. Lebensohn, F. Roters, *Int. J. Plast.* 46 (2013) 37–53.
- [36] F. Vercruyse, C. Celada-Casero, B.M. Linke, P. Verleysen, R.H. Petrov, *Mater. Sci. Eng., A* 800 (2021) 140293.
- [37] C.F. Jateczak, *SAE Int.* (1980) 1657–2676.
- [38] J.B. Nelson, D.P. Riley, *Proc. Phys. Soc.* 57 (1945) 160–177.
- [39] C.K. Lowe-Ma, W.T. Donlon, W.E. Dowling, *Powder Diffraction* 16 (2012) 198–204.
- [40] N.H. van Dijk, A.M. Butt, L. Zhao, J. Sietsma, S.E. Offerman, J.P. Wright, S. van der Zwaag, *Acta Mater.* 53 (2005) 5439–5447.
- [41] Y. Toji, G. Miyamoto, D. Raabe, *Acta Mater.* 86 (2015) 137–147.
- [42] A. Smith, F. Vercruyse, R. Petrov, P. Verleysen, *J. Phys. Conf.* 1270 (2019), 012030.
- [43] T. Gladman, *The Physical Metallurgy of Microalloyed Steels*, Maney for the Institute of Materials, 2002.
- [44] R.-M. Rodriguez, I. Gutierrez, *Mater. Sci. Forum* 426–432 (2003) 4525–4530.
- [45] K. Sugimoto, M. Mukherjee, 8 - TRIP aided and complex phase steels, in: R. Rana, S.B. Singh (Eds.), *Automotive Steels*, Woodhead Publishing, 2017, pp. 217–257.
- [46] G.I. Taylor, *Proc. R. Soc. Lond. - Ser. A Contain. Pap. a Math. Phys. Character* 145 (1934) 362–387.
- [47] T. Gladman, *Mater. Sci. Technol.* 15 (1999) 30–36.
- [48] G. Ghosh, G.B. Olson, *Acta Mater.* 50 (2002) 2099–2119.
- [49] J.M. Rosenberg, H.R. Piehler, *Met. Trans.* 2 (1971) 257–259.
- [50] S.C. Kennett, G. Krauss, K.O. Findley, *Scripta Mater.* 107 (2015) 123–126.
- [51] S.Y.P. Allain, S. Aoued, A. Quintin-Poulon, M. Gouné, F. Danoix, J.-C. Hell, M. Bouzat, M. Soler, G. Geandier, *Materials* 11 (2018) 1087.
- [52] J. Gil-Sevillano, in: P.H.a.E.J.K.R. W. Cahn (Ed.), *Flow Stress and Work Hardening*, *Mater. Sci. Tech.*, 1993, pp. 19–88.
- [53] J. Gil-Sevillano, *Flow stress and work hardening*, *Mater. Sci. Technol.* (2006).
- [54] F. Maresca, V.G. Kouznetsova, M.G.D. Geers, *J. Mech. Phys. Solid.* 73 (2014) 69–83.
- [55] A. Arlazarov, O. Bouaziz, A. Hazotte, M. Gouné, S. Allain, *ISIJ Int.* 53 (2013) 1076–1080.
- [56] L.R.C. Malheiros, E.A.P. Rodriguez, A. Arlazarov, *Mater. Sci. Eng., A* 706 (2017) 38–47.
- [57] G. Krauss, *Mater. Sci. Eng., A* 273–275 (1999) 40–57.
- [58] D. Raabe, D. Ponge, O. Dmitrieva, B. Sander, *Scripta Mater.* 60 (2009) 1141–1144.
- [59] S. Peng, Y. Wei, H. Gao, *Proc. Natl. Acad. Sci. Unit. States Am.* 117 (2020) 5204–5209.